



## Comparative study of LiMnPO<sub>4</sub>/C cathodes synthesized by polyol and solid-state reaction methods for Li-ion batteries

Nicholas P.W. Pieczonka <sup>a,b</sup>, Zhongyi Liu <sup>c</sup>, Ashfia Huq <sup>d</sup>, Jung-Hyun Kim <sup>a,\*</sup>

<sup>a</sup>Chemical & Materials Systems Laboratory, General Motors Global R&D Center, Warren, MI 48090, USA

<sup>b</sup>Optimal CAE Inc, Plymouth, MI 48170, USA

<sup>c</sup>Electrochemical Energy Research Laboratory, General Motors Global R&D Center, Warren, MI 48090, USA

<sup>d</sup>Neutron Scattering Science Division, Oak Ridge National Laboratory, Oak Ridge, TN 37831, USA

### HIGHLIGHTS

- Effect of synthetic methods on LMP was investigated.
- LMP had 4–5% cation mixing from powder neutron diffraction data.
- TEM analysis showed that polyol method grows LMP platelets parallel to *bc*-plane.
- Polyol method with super-P composite offered the best performances.
- Capacity of LMP was strongly influenced by upper cut-off voltage used.

### ARTICLE INFO

#### Article history:

Received 14 August 2012

Received in revised form

24 November 2012

Accepted 6 December 2012

Available online 20 December 2012

#### Keywords:

Olivine

LiMnPO<sub>4</sub>

Solid-state reaction method

Polyol method

Carbon composite

### ABSTRACT

A systematic comparison of LMP prepared by solid-state reaction (SSR) and polyol methods was carried out through detailed analyses that included: X-ray and neutron powder diffractions, scanning electron microscopy (SEM), transmission electron microscopy (TEM), and electrochemical characterization. The LMP synthesized by the two different methods had a similar amount of Li/Mn cation mixing, ca. 4–5%. The polyol method provided a flower-like morphology to the LMP particles, in the form of platelet of which growth direction is parallel to the *bc*-plane. The LMP prepared by the polyol method was further optimized by carbon composite using two different kinds of carbon sources: Shawinigan acetylene black (AB) and Super-P Li carbon black (SP). With the smallest crystallite size and a homogeneous carbon particle network, the LMP processed with SP delivered better cathode performance than both the AB – mixed LMP and that prepared by the SSR method. AC-impedance spectroscopy of the LMP composite with SP showed an abrupt increase in impedance after 50% delithiation. Because of this difficulty of charging, the capacity of the LMP composite with SP was strongly influenced by the upper cut-off voltage used.

© 2012 Elsevier B.V. All rights reserved.

## 1. Introduction

The olivine-structured LiFePO<sub>4</sub> (LFP) has emerged as a viable positive electrode material for Li-ion batteries [1]. It has demonstrated properties of safety, stability, and cyclability while having good specific capacity and energy density [1]. Intrinsically, LFP has the material characteristics of an insulator with low ionic ( $\sigma_{\text{ion}} = 1.9 \times 10^{-9} \text{ S cm}^{-1}$  at 147 °C along the *b*-axis) and electronic ( $\sigma_{\text{electron}} \sim 7.5 \times 10^{-9} \text{ S cm}^{-1}$  at 40 °C along the *a*-axis) conductivities

[2]. Fortunately, two material innovations have been achieved that improve the potential for LFP to be a viable electrode material for electric vehicle (EV) applications: i) the use of carbon composites to improve electronic conductivity and ii) a reduction of the effective primary particle size to the nanometer regime to compensate for the low ionic conductivity. However LFP delivers a relatively low operating voltage of ~3.5 V (vs. Li<sup>+</sup>/Li<sup>0</sup>) compared with other positive electrode materials such as LiCoO<sub>2</sub> and Li<sub>1+x</sub>Mn<sub>2-x</sub>O<sub>4</sub>. This remains a disadvantage of LFP and has motivated investigations into materials that have many of the positive aspects of the olivine system but with improved energy density and capacity.

LiMnPO<sub>4</sub> (LMP) offers a higher operating voltage of 4.1 V (vs. Li<sup>+</sup>/Li<sup>0</sup>) compared with that of LFP [3]. Fig. 1 illustrates the crystal

\* Corresponding author. Tel.: +1 586 335 0509.

E-mail address: [junghyun.kim@gm.com](mailto:junghyun.kim@gm.com) (J.-H. Kim).

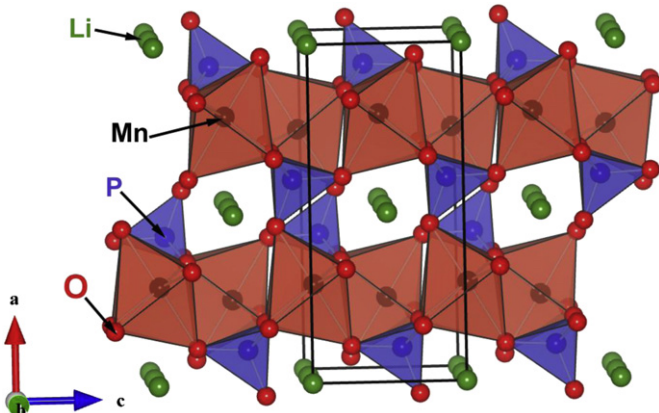


Fig. 1. Crystal structure of  $\text{LiMnPO}_4$ . Solid lines indicate a unit cell.

structure of LMP, which is orthorhombic, with a space group of  $Pnma$ , referred to as the olivine structure [3]. The crystal lattice of LMP consists of corner-sharing  $\text{MnO}_6$  octahedra and edge-sharing  $\text{LiO}_6$  octahedra that are linked by  $\text{PO}_4$  tetrahedra. The  $\text{Li}^+$  pathway in the olivine crystal structure of these materials is one-dimensional, parallel to the  $b$ -axis as seen in Fig. 1 [4]. LMP is an appealing alternative to LFP because it provides a higher operating voltage, and a ~20% higher gravimetric energy density as can be seen in Table 1 (along with the physical and electrochemical properties of LMP and those of LFP).

There are, however, additional challenges with LMP such as lower electrical conductivity and being less amenable to carbon coating methods compared to LFP [5]. For example, LMP has more difficulty in forming effective conductive carbon coatings due to the less reactive nature of Mn, relative to Fe, to carbon sources. It has been suggested that the rate limiting factor in LMP is low electrical conductivity rather than the ionic conductivity [4]. There are several approaches to improve the performance of LMP. An important approach is to reduce the crystallite size and modify the primary and secondary particle morphology so as to minimize the length of the  $\text{Li}^+$  conduction channels [6]. An ideal morphology would have the shortest dimension along the  $b$ -axis. Control of crystal morphology and growth has been shown to be possible with soft-chemistry synthetic routes such as sol–gel, polyol, hydrothermal, and microwave synthesis [6–9]. Particularly attractive is the polyol method which allows the synthesis of inorganic nanoparticles without further heat-treatment [7]. Traditional solid-state synthesis routes also have been used to prepare LMP though these approaches provide limited control over particle size and morphology [10]. However, a solid-state synthesis route does have the benefit of an easier scale-up than a polyol route. In this paper, two synthesis methods, a solid-state procedure and a polyol reaction, were explored to better understand the role of factors such as preparation method, particle size, and particle morphology have on the electrochemical performance of LMP.

**Table 1**  
Comparison of  $\text{LiFePO}_4$  and  $\text{LiMnPO}_4$ .

Properties	$\text{LiFePO}_4$	$\text{LiMnPO}_4$
Density ( $\text{g cm}^{-3}$ )	3.7	3.4
Theoretical gravimetric capacity ( $\text{mAh g}^{-1}$ )	170	171
Theoretical volumetric capacity ( $\text{mAh cm}^{-3}$ )	629	581
Operation voltage (vs. $\text{Li}^+/\text{Li}^0$ ) (V)	3.45	4.1
Theoretical gravimetric energy density ( $\text{Wh kg}^{-1}$ )	586	701
Theoretical volumetric energy density ( $\text{Wh L}^{-1}$ )	2170	2384
Electrical conductivity ( $\text{S cm}^{-1}$ )	$\sim 10^{-9}$	$< 10^{-10}$

## 2. Experimental

### 2.1. Polyol synthesis method

LMP was formed via a modified polyol synthesis in which stoichiometric amounts of  $\text{Mn}(\text{CH}_3\text{COO})_2 \cdot 4\text{H}_2\text{O}$  (Mn-Ace) and  $\text{LiH}_2\text{PO}_4$  (Sigma–Aldrich), were combined using ethylene glycol (EG) as the solvent. The EG acts both as a chelating agent and as a mild reducing agent to the  $\text{Mn}^{2+}$  ions. In a typical reaction, 150 mL of ethylene glycol is added to a 250 mL 3-neck round bottom flask with a condenser and stir-bar, and heated to 100 °C to which 0.03 mol of Mn-Ace was added and heated ~100 °C for 20 min. Formation of a deep ruby-colored solution indicated the complete dissolution of the Mn-Ace. 15 mL (0.03 mol) of a 1 M  $\text{LiH}_2\text{PO}_4$  aqueous solution was then added drop wise under constant stirring conditions at a rate of less than 1  $\text{mL min}^{-1}$  via a syringe. The mixture was heated at 135 °C, under reflux and constant stirring for 4 h. The final product was obtained by transferring the solution into centrifuge tubes which were centrifuged at 4000 rpm for 20 min. The supernatant was removed and the sediment was re-dispersed in ethanol and centrifuged again. This process was repeated until the supernatant was clear. The resulting gel was then filtered (0.8  $\mu\text{m}$  Nylon Membrane Filters) and washed with ethanol followed with a final rinse of acetone. The remaining solid was then heated under vacuum at 120 °C overnight.

To attain any usable capacity from phosphate-based materials, particles must have layer of conductive carbon or be intimately embedded in a conductive carbon network. A number of ways to achieve this have been presented in the literature [11]. Among them, one of the most effective is high-energy ball milling of the LMP material with a carbon source. This method was adapted for this work [3]. Two carbon black sources were used: Shawinigan acetylene black (Chevron Philips Acetylene Black) (AB) and Super-P Li carbon black (Timcal) (SP). A 20 wt% ratio of carbon to LMP was used. The mixture was transferred to a stainless steel vessel for planetary ball milling with stainless steel balls, and a ball mass ratio of 5:1 was used. The mixture was milled at 300 rpm for 4 h.

### 2.2. Solid-state reaction synthesis method

LMP was also synthesized via a solid-state reaction method [10]. Stoichiometric amounts of  $\text{Li}_2\text{CO}_3$ ,  $\text{MnCO}_3$ , and  $(\text{NH}_4)_2\text{HPO}_4$  (Sigma–Aldrich) precursors were mixed with super-P carbon black (Timcal) (SP) to produce 2.5 g (0.0159 mol) of LMP with 20 wt% carbon. The carbon provides two functions: i) to provide the carbon source for the necessary conductive carbon network and ii) to limit phosphate particle growth during the synthesis. The precursors were loaded into a stainless steel vessel for planetary ball milling (80 mL) with stainless steel balls with reactants to ball mass ratio of 20:1. The container and contents were then subjected to high-energy ball milling in a Fritch planetary ball mill (Fritch 4000). The duration of this milling was 12 h at 300 rpm. The milled powder was collected and reground. The powder was then heated at 550 °C for 6 h in an  $\text{Ar}/3\% \text{H}_2$  atmosphere in a tube furnace (5 °C  $\text{min}^{-1}$  heating and cooling rate). The final material was of a mix of LMP particles embedded in a carbon network and no further carbon treatment was needed.

### 2.3. Material characterization

Powder X-ray diffraction (XRD) measurements were carried out with a Bruker D8 diffractometer with  $\text{Cu}-\text{K}_{\alpha 1}$  radiation in Bragg–Brentano configuration. Powder neutron diffraction measurements were conducted at POWGEN diffractometer (beamline 11A) at the Spallation Neutron Source at Oak Ridge National Laboratory.

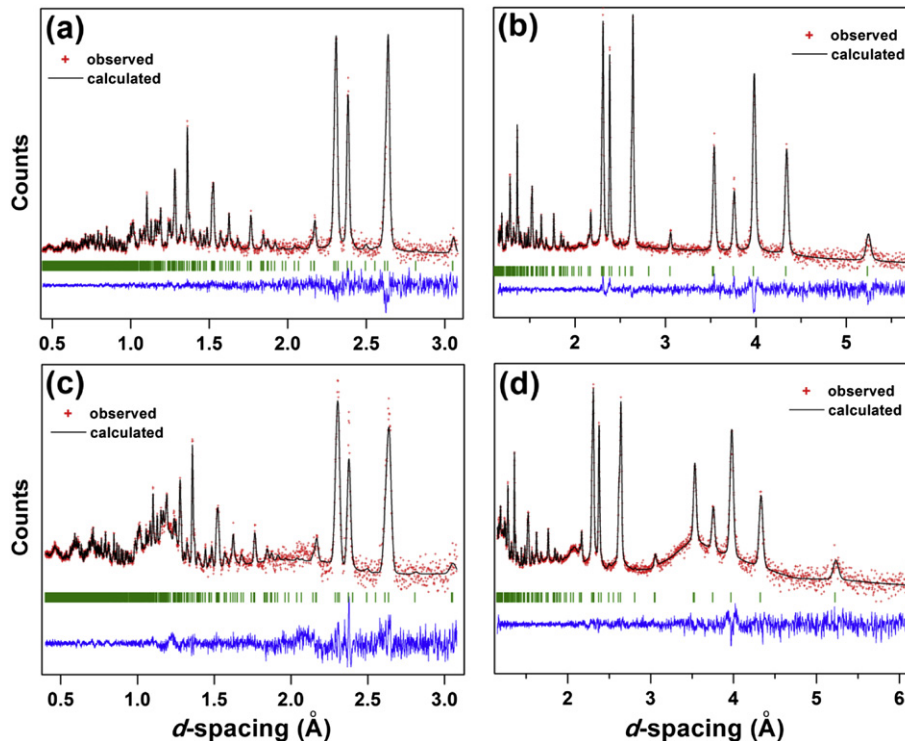


**Fig. 2.** Rietveld refinement profiles of powder neutron diffraction data for (a,b)  $\text{LiMnPO}_4$  synthesized by the polyol method, and (c,d)  $\text{LiMnPO}_4 + \text{C}$  composite synthesized by the solid-state reaction (SSR) method. Neutron diffraction data were collected using two different center wavelengths to access different  $d$ -spacing ranges. Green tick marks and the blue line below the pattern, respectively, show the positions of the Bragg peaks and the difference between observed and calculated patterns. The  $\text{LiMnPO}_4 + \text{C}$  composite sample showed higher background coming from the carbon in (c) and (d). (For interpretation of the references to colour in this figure legend, the reader is referred to the web version of this article.)

The resulting neutron diffraction data were refined via Rietveld method using the GSAS program [12,13]. Scanning electron microscopy (SEM) images were acquired with a JEOL Gemini, and transmission electron microscopy (TEM) analysis was performed with an aberration-corrected JEOL JEM-2100F operated at 200 kV. Samples suitable for TEM observation were prepared by grinding the as-synthesized powder between two clean glass slides and then dusting the ground fine powder onto lacy-carbon-coated Cu TEM grids. Electron diffraction patterns were indexed using the Java version of the electron microscopy simulation (JEMS) program [14]. Electrochemical cycling studies were conducted on a Macor 4000 battery testing system.

Electrodes were fabricated from composite slurry consisting of a 75:20:5 wt% mix of active material, super-P carbon, and polyvinylidene fluoride (PVDF), with 1.5 mL of *N*-methyl-pyrrolidone (NMP). This slurry was mixed with a stir-bar (600 rpm) in a 20 mL glass vial overnight. The resulting slurry was spread via doctor-blade method ( $\sim 200 \mu\text{m}$ ) onto Al-foil (23  $\mu\text{m}$  thick). The cast material was allowed to dry for 2 h in a fume-hood and then was transferred to a vacuum oven set at 120 °C to dry overnight. The dried sheet was then pressed from a starting thickness  $\sim 80 \mu\text{m}$  to a final thickness of 25  $\mu\text{m}$ . 13 mm diameter electrodes were punched for later use in coin cells. Coin cells (Hohsen Co. 2032 model) were assembled in an argon-filled glove box in half-cell configuration using a 17 mm diameter lithium foil as the counter/reference electrode, a separator (Cel-guard), and a 1 M  $\text{LiPF}_6$  in EC:DEC (1:2 vol. ratio) electrolyte. AC-impedance spectroscopy (Solartron 1287/1260 FRA) of the half-cell was measured at different states of charge at room temperature. The resulting spectra were fitted using ZView software (Scribner Inc.).

### 3. Results and discussion

#### 3.1. Material characterization

The crystal structures of LMP powders synthesized by polyol and solid-state reaction methods were analyzed by neutron and X-ray diffraction. The LMP prepared by the polyol method (denoted by LMP-Pol hereafter) had a platelet morphology (will be discussed later) that resulted in significant preferred orientation effects in the XRD data. Due to the larger sampling volume allowed

**Table 2**  
Structural parameters of the  $\text{LiMnPO}_4$  (LMP).

Elements	X	Y	Z	Occupancy
LMP synthesized by the polyol method				
$\text{Li}/\text{Mn}_2$	0	0	0	0.955 (18)/0.045 (18)
$\text{Mn}_1/\text{Li}_2$	0.2193 (3)	1/4	0.5301 (8)	0.955 (18)/0.045 (18)
P	0.4079 (3)	1/4	0.0940 (4)	1
O <sub>1</sub>	0.0456 (2)	1/4	0.2899 (5)	1
O <sub>2</sub>	0.4019 (2)	1/4	0.7733 (5)	1
O <sub>3</sub>	0.3380 (2)	0.0481 (2)	0.2246 (3)	1
Space group: <i>Pnma</i> lattice parameters are $a = 10.4475 \text{ \AA}$ , $b = 6.1049 \text{ \AA}$ , $c = 4.7469 \text{ \AA}$ , $R_p = 6.12\%$ , $R_{wp} = 3.03\%$ , $\chi^2 = 1.543$ .				
LMP-C synthesized by the solid-state reaction method				
$\text{Li}/\text{Mn}_2$	0	0	0	0.956 (28)/0.044 (28)
$\text{Mn}_1/\text{Li}_2$	0.2174 (5)	1/4	0.5294 (12)	0.956 (28)/0.044 (28)
P	0.4084 (4)	1/4	0.0903 (6)	1
O <sub>1</sub>	0.0444 (2)	1/4	0.2878 (7)	1
O <sub>2</sub>	0.4024 (3)	1/4	0.7707 (6)	1
O <sub>3</sub>	0.3378 (2)	0.0492 (3)	0.2235 (5)	1
Space group: <i>Pnma</i> lattice parameters are $a = 10.4690 \text{ \AA}$ , $b = 6.0996 \text{ \AA}$ , $c = 4.7579 \text{ \AA}$ , $R_p = 4.97\%$ , $R_{wp} = 2.65\%$ , $\chi^2 = 1.421$ .				

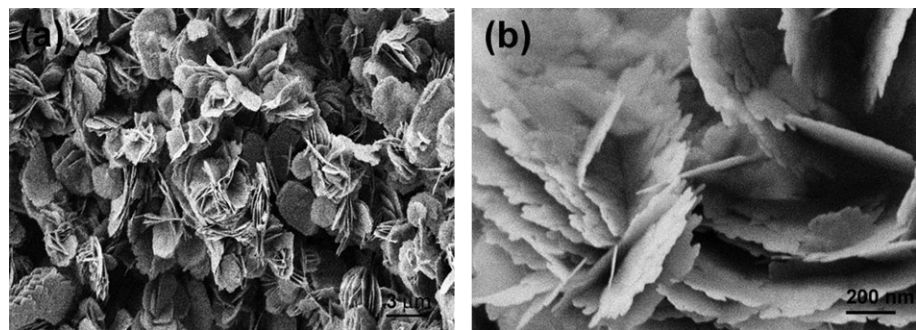


**Fig. 3.** Scanning electron microscope (SEM) images of LiMnPO<sub>4</sub> (LMP) synthesized by the polyol method.

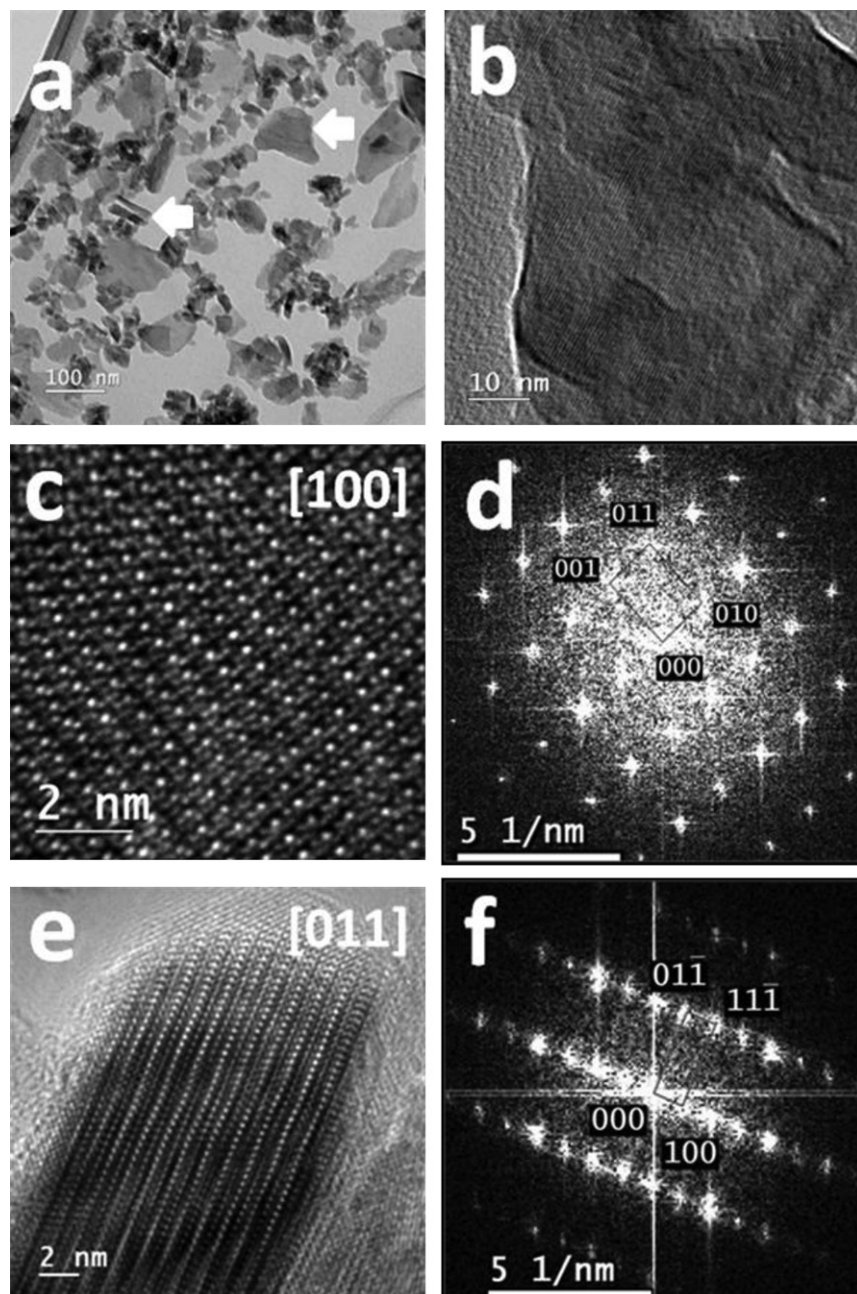


**Fig. 4.** Typical TEM images of LiMnPO<sub>4</sub> (LMP) synthesized by the polyol method; (a) Image showing platelet-like LMP “face-on” (parallel to the platelet’s normal) and “edge-on” (perpendicular to the platelet’s normal) directions; (b,c) Low- and high-magnification images of one platelet oriented in the “face-on” direction; (d) A diffractogram obtained via fast Fourier transform (FFT) of (c) showing that the “face-on” direction is parallel to the [100] zone axis of LMP; (e) High-magnification image of one platelet oriented in “edge-on” direction; and (f) A diffractogram of (e) showing that the “edge-on” direction is parallel to the [011] zone axis of LMP.

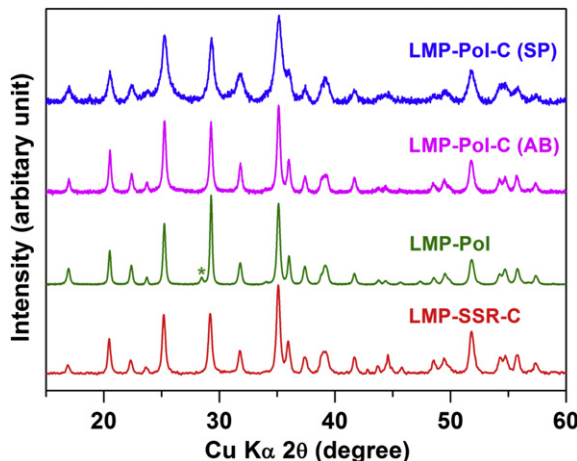


**Fig. 5.** XRD patterns of  $\text{LiMnPO}_4$  (LMP) synthesized by the polyol method before and after carbon composite and by the solid-state reaction method. Reflection from Si internal reference is marked with \*.

**Table 3**  
Lattice parameters and crystallite sizes of  $\text{LiMnPO}_4$  (LMP).

Samples	$a$ ( $\text{\AA}$ )	$b$ ( $\text{\AA}$ )	$c$ ( $\text{\AA}$ )	Crystallite <sup>a</sup> size (nm)
LMP-SSR-C	10.448	6.105	4.747	29
LMP-Pol	10.469	6.100	4.758	37
LMP-Pol-C (SP)	10.475	6.095	4.746	14
LMP-Pol-C (AB)	10.463	6.104	4.751	30

<sup>a</sup> Determined by use of the Scherrer equation.

for neutron diffraction, the LMP particles are more randomly oriented in the sample container used, and hence the data did not suffer from the effects of preferred orientation making the structural analysis less complicated. Fig. 2 shows the powder neutron

diffraction data of the LMP–Pol powders and their refinements based on an orthorhombic structure with a space group of  $Pnma$ . This orthorhombic structure model allowed satisfactory fitting of the neutron diffraction data of the LMP–Pol samples without the need to correct for any preferred orientation. However anisotropic strain parameters [15], had to be used which offered significant improvement in the quality of fits. The resulting structural parameters and the quality of refinement are listed in Table 2.

The LMP synthesized by the solid-state reaction method (denoted by LMP–SSR–C hereafter) contains carbon which was introduced during the synthetic process and which contributed to the background intensity in Fig. 2(c) and (d). During the structure refinement, occupancies of Li and Mn at two different octahedral interstitial sites were carefully examined. The results showed that both LMP–Pol and LMP–SSR–C samples have a similar amount of cation mixing of about 4–5% between Li and Mn (see Table 2). The amount of cation mixing is important because any  $\text{Mn}^{2+}$  present in a  $\text{Li}^+$  site will block the  $\text{Li}^+$  diffusion channel along the  $b$ -axis and will lead to a subsequent decrease in electrochemical capacity due to the nature of the one-dimensional  $\text{Li}^+$  diffusion pathway. An earlier study reported that LFP synthesized at 120 °C by hydrothermal method had 8% of Li/Fe cation mixing though it was negligible after heating at  $T > 200$  °C [16]. In contrast, LFP synthesized at 850 °C by the sol-gel method still had approximately 3–6% of cation mixing that varied depending on the synthesis conditions [17]. It is interesting to note that the LMP obtained by the polyol method at the relatively low temperature of 135 °C had a similar low amount of cation mixing as that obtained by the solid-state reaction method at 550 °C.

Fig. 3 shows the plate-like of the particles of the LMP–Pol samples. The SEM image in Fig. 3(a) shows large clusters of particles (nominal diameters of a few micrometers) with flower-like morphology. At higher magnification in Fig. 3(b), however, it can be seen that the

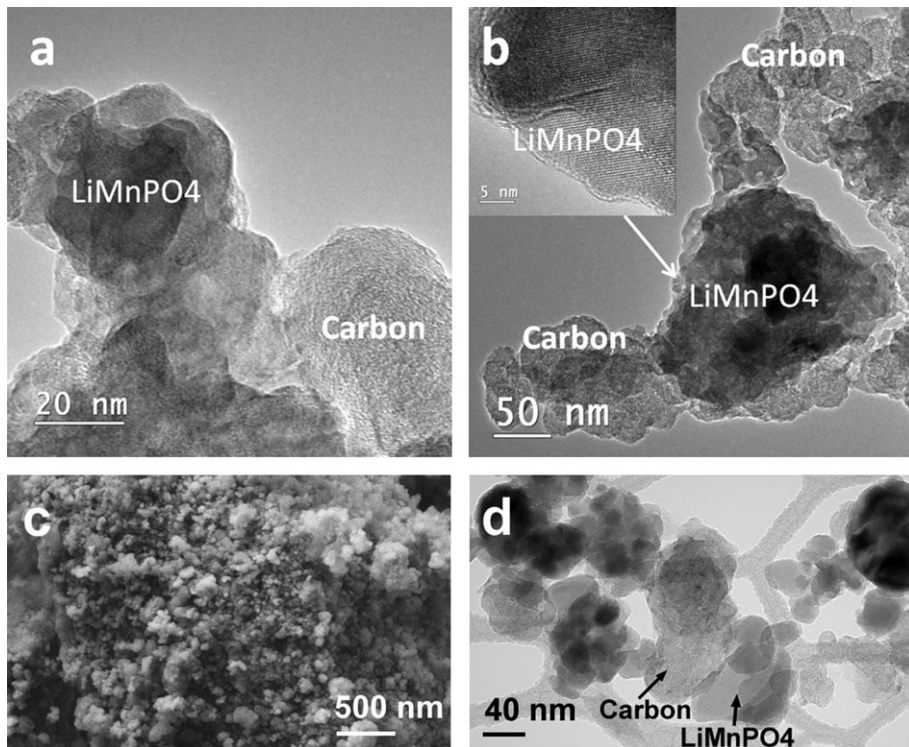


**Fig. 6.** Typical TEM and SEM images showing various mixtures of  $\text{LiMnPO}_4$  (LMP) and carbon nanoparticles; (a) TEM image of LMP–SSR–C; (b) TEM image of LMP–Pol–C (SP); (c) SEM image of LMP–Pol–C (AB); and (d) TEM image of LMP–Pol–C (AB).

larger plate structure comprises assemblies of smaller domains (platelets). Dimensional analysis indicated that the larger plate's structures were on the micrometer order, both in width and length, with thicknesses of less than 100 nm. The smaller domains were on the order of tens of nanometers and thicknesses less than 50 nm.

TEM was used to further observe the structural characteristics of the "flower-like" hierarchical microstructure of the LMP–Pol crystals seen in the SEM images. The growth direction was determined under an assumption that the normal of the LiMnPO<sub>4</sub> platelets observed in the TEM is parallel to the normal of the petals of the flower-like LiMnPO<sub>4</sub> crystals. In Fig. 4, platelets that were oriented in "face-on" (parallel to the platelet's normal) and "edge-on" (perpendicular to the platelet's plane) directions were imaged and their diffractograms (obtained by fast Fourier transform of TEM images) were indexed. The "face-on" and "edge-on" directions correspond to [100] and [011] zone axes, respectively. Based on the indexed zone axes, it is concluded that the growth direction of the LiMnPO<sub>4</sub> crystal is along its [100] zone axis. In other words, the wide platelets shown in Fig. 4(b) are parallel to the *bc*-plane while the direction of the thin layer (~20 nm thickness) in Fig. 4(e) is parallel to the *a*-axis. This result agrees well with recent reports in the literature [18].

### 3.2. Effect of carbon composites

The LMP–Pol sample needs additional processing to incorporate the LMP particles in a conductive carbon network to overcome the intrinsic insulating properties of LMP, whereas the LMP–SSR–C as stated early sample does not. The LMP–Pol powder was ground with either Super-P Li carbon black (SP) or Shawinigan acetylene black (AB) using planetary ball milling for 4 h. This carbon composite process also provides a critical benefit of decreasing particle sizes of the LMP–Pol powder and of consequently reducing the Li<sup>+</sup> diffusion length along the *b*-axis. It has been understood that the breaking of particles increases the amount of less-coordinated atoms at surfaces of both LMP and the carbon source which can promote a homogeneous carbon/LMP network [19]. Fig. 5 compares XRD patterns of the LMP–Pol powders (before and after the carbon composite procedure) and the as-prepared LMP–SSR–C powder. The pristine LMP–Pol has crystallite size of 37 nm as determined by the Scherrer equation in Table 3. Meanwhile, the carbon composite of LMP–Pol using Shawinigan Acetylene Black [hereafter denoted by LMP–Pol–C (AB)] showed slightly broader reflections from XRD with a crystallite size of 30 nm, which is very close to 29 nm obtained from the LMP–SSR–C powder (Table 3). It is interesting to note that carbon composite using the Super-P [hereafter denoted by LMP–Pol–C (SP)] resulted in the smallest crystallite size of 14 nm with broad XRD reflections characteristic of nano-sized particles.

Fig. 6 demonstrates the effect of the carbon processing on the LMP particles. In Fig. 6(a), the LMP–SSR–C sample shows that the final product consists of agglomerations of 20–30 nm particles of carbon and LMP. As seen in Fig. 6(c), the representative SEM image obtained from the LMP–Pol–C (AB) powder shows a severe agglomeration of primary particles without any of the flower-like morphology, which was characteristic of the pristine LMP–Pol sample (Fig. 3). The HR-TEM image in Fig. 6(b) reveals the intimate mixing of carbon and LMP in the LMP–Pol–C (SP). Crystalline cores of LMP can be seen with ~30 nm diameters though individual particle sizes are hard to estimate due to the agglomeration of LMP and SP particles. In contrast, the LMP–Pol–C (AB) sample consists of larger LMP particles that are more segregated from the AB carbon aggregates, as shown in Fig. 6(d). Earlier studies have reported that AB carbon particles are approximately two times larger than that of SP (~40 nm) as assessed by TEM [20,21]. More importantly, it has been reported that the AB carbon has a concentric graphene-like outer shell that may make it resistant to

attrition by ball milling [22]. This helps explain the less effective mixing of carbon and the larger crystallite size of the milled LMP–Pol–C (AB) compared with those of the LMP–Pol–C (SP).

### 3.3. Electrochemical properties

The electrochemical performances of LMP–Pol–C (SP), LMP–Pol–C (AB), and LMP–SSR–C were evaluated with coin-type half-

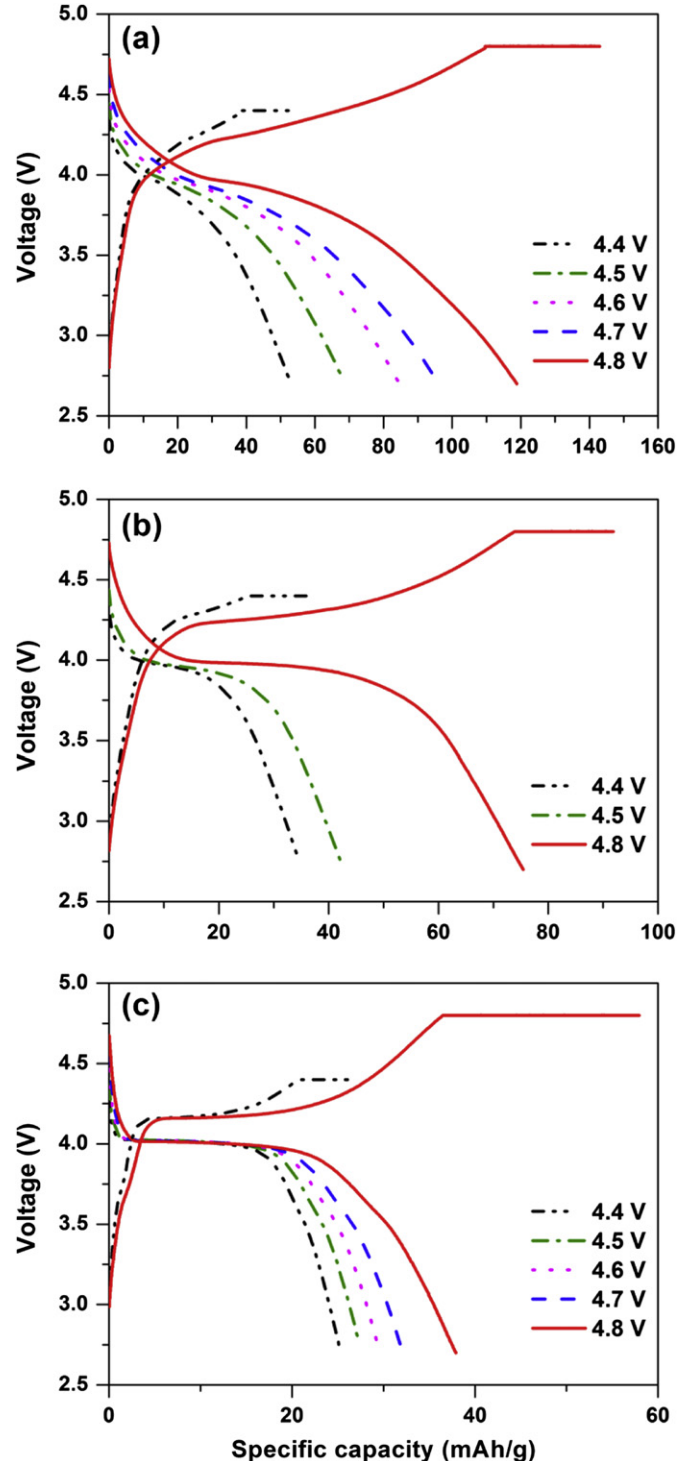


Fig. 7. Discharge profiles of (a) LMP–Pol–C (SP), (b) LMP–Pol–C (AB), and (c) LMP–SSR–C cathodes measured using half-cells by applying constant current density of 8.55 mA g<sup>−1</sup> with different upper cut-off voltages of 4.4–4.8 V at 30 °C.

cells using Li as the anode. The half-cells were charged using a constant current (CC)—constant voltage (CV) method followed by CC discharge; charged with a constant rate of  $8.55 \text{ mA g}^{-1}$  followed by dwelling at a specific upper cut-off voltage until the current decay reached  $1.7 \text{ mA g}^{-1}$ , and then discharged at the constant current density of  $8.55 \text{ mA g}^{-1}$ . Fig. 7 shows the discharge profiles of the three different cathodes with varying upper cut-off voltages of 4.4–4.8 V. Their corresponding C-rates were approximately in a range of C/3–C/13. It was found that the discharge capacities strongly influenced by the upper cut-off voltage used. For example, the capacity attained at 4.4 V was  $47 \text{ mAh g}^{-1}$ , while that measured at 4.8 V was  $120 \text{ mAh g}^{-1}$  from the LMP-Pol-C (SP) cathode.

Similarly, cathodes prepared from the other experimental materials also exhibited the behavior of increasing discharge capacity with increasing upper cut-off voltage. This behavior is summarized in Fig. 8. The LMP-Pol-C (SP) cathode delivered higher capacity than did the LMP-Pol-C (AB) cathode at each given upper cut-off voltage. The LMP-SSR-C cathode delivered the lowest discharge capacity of  $40 \text{ mAh g}^{-1}$  with the upper cut-off voltage of 4.4 V. Again larger capacities were achieved with higher cut-off voltage though the effect was not nearly as dramatic as with the LMP-Pol-C (SP). The high cut-off voltage required to obtain larger capacities can be understood by considering the large polarization between charge and discharge due to the intrinsic insulating properties of LMP [10]. In addition, the difficulty in charging of LMP has been attributed to structural limitations such as lattice contraction and/or structural instability mainly related to a partial spin-state transition of  $\text{Mn}^{3+}$  from high to low spin during delithiation and subsequent local strains in the lattice [23].

The AC-impedance spectra of LMP-Pol-C (SP)/Li cells were measured at different states of charge. Fig. 9(a) illustrates the charge profile with intermittent rests followed by AC-impedance measurements at different values of  $x$  in  $\text{Li}_{1-x}\text{MnPO}_4$  (marked with red circles). The representative impedance spectra are shown in Fig. 9(c). Each spectrum was fitted based on an equivalent circuit model which consisted of the following elements:

$$R_s - (R_1/\text{CPE}_1) - (R_2/\text{CPE}_2) - W_0 - C, \quad (1)$$

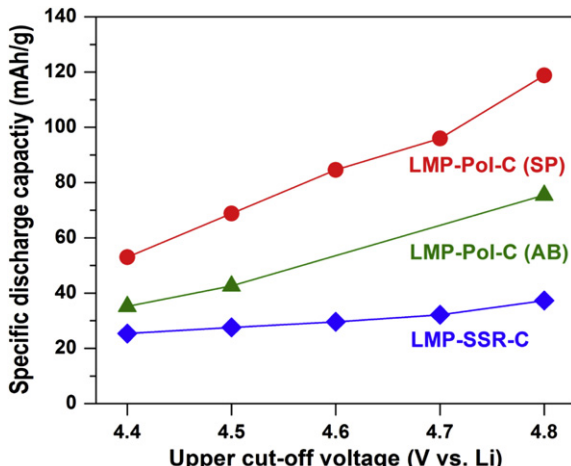


Fig. 8. Comparison of discharge capacity as a function of upper cut-off voltage for LMP-Pol-C (SP), LMP-Pol-C (AB), and LMP-SSR-C cathodes measured using half-cells at  $30^\circ\text{C}$ .

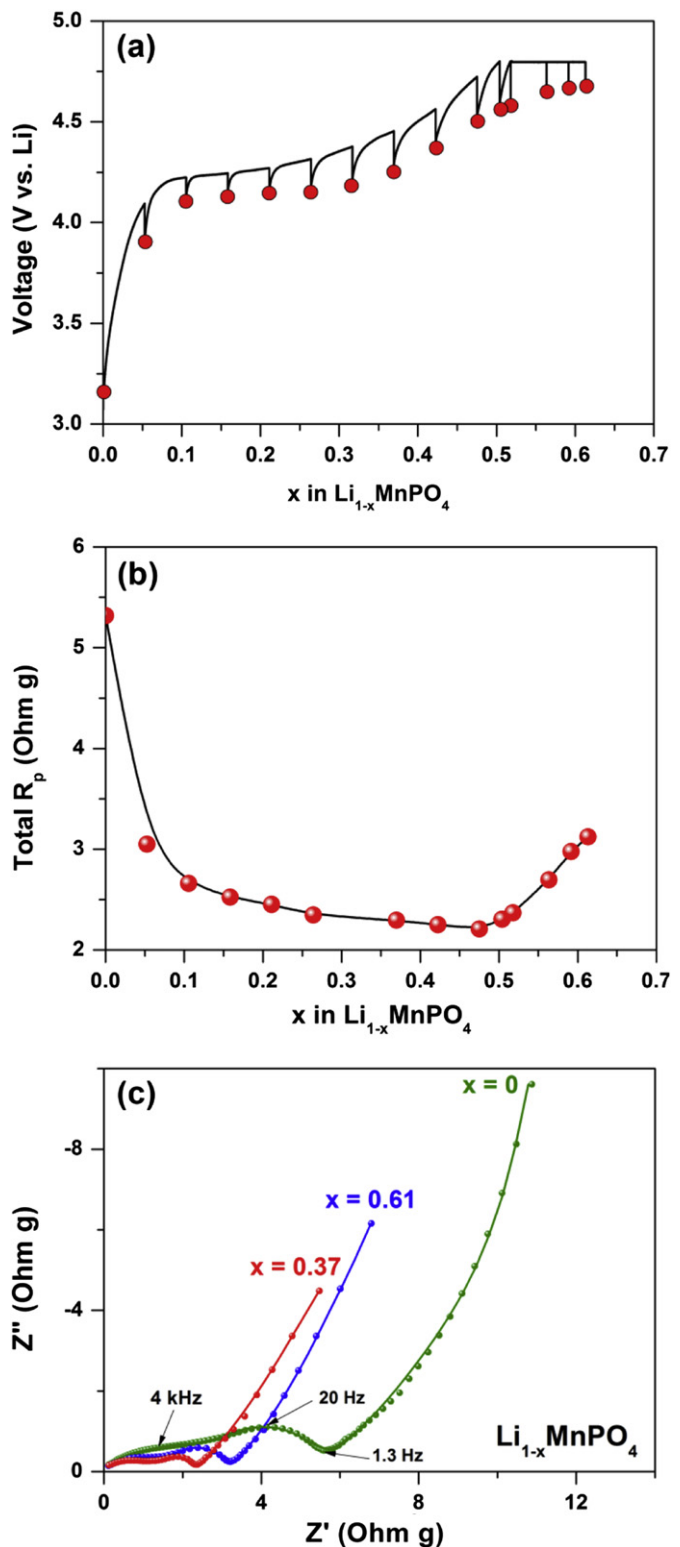
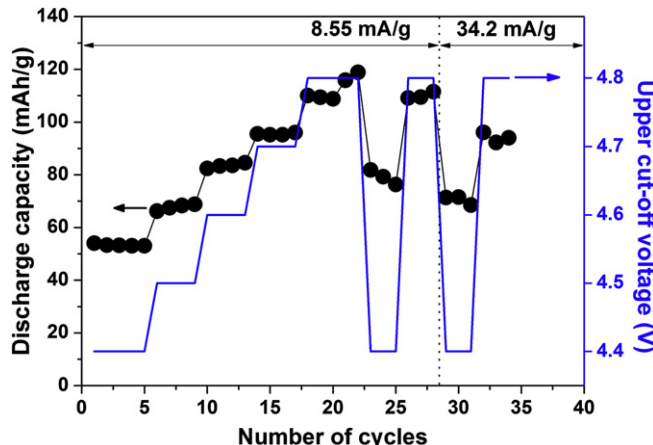


Fig. 9. (a) Charge profile with intermittent rests followed by AC-impedance measurement at different  $x$  in  $\text{Li}_{1-x}\text{MnPO}_4$  (marked with red circle) obtained from LMP-Pol-C (SP) cathode, (b) Normalized total  $R_p$  as a function of  $x$  in  $\text{Li}_{1-x}\text{MnPO}_4$ , and (c) representative observed (plot) and fitted (line) AC-impedance spectra recorded at  $x = 0, 0.37$ , and  $0.61$  in  $\text{Li}_{1-x}\text{MnPO}_4$ . (For interpretation of the references to colour in this figure legend, the reader is referred to the web version of this article.)



**Fig. 10.** Variation of discharge capacity of LMP-Pol-C (SP) cathode with upper cut-off voltages and current densities at 30 °C. The applied current densities are shown. The cell was charged with CC–CV method as described in the text.

where  $R_s$  is attributed to the resistance of the electrolyte, ( $R_1/CPE_1$ ) is associated with the charge-transfer process from electrolyte to LMP, ( $R_2/CPE_2$ ) will be related to the interfacial resistance/capacitance between LMP particles,  $W_0$  appearing in the low frequency region belongs to the  $\text{Li}^+$  diffusion in LMP bulk, and  $C$  is a capacitance blocking  $\text{Li}^+$  at the current collector [3,24]. From the fitting results, the variation of total  $R_p$  as a function of  $x$  in  $\text{Li}_{1-x}\text{MnPO}_4$  is plotted in Fig. 9(b). On charging, it shows a steady decrease in  $R_p$  for  $0.1 < x < 0.5$  followed by an abrupt increase in  $R_p$  for  $x > 0.5$ . This increasing impedance after 50% of charging indicates the difficulty of delithiation partly due to the aforementioned lattice strains in LMP.

The LMP-Pol-C (SP)/Li cell was cycled with different upper cut-off voltages and current densities. Fig. 10 shows the variation of discharge capacity obtained under these various conditions. During the first 22 cycles, the upper cut-off voltages of the cell were increased from 4.4 to 4.8 V. In agreement with earlier data, the LMP-Pol-C (SP) cathode delivered increasing capacity with higher upper cut-off voltage. When the cut-off voltage was decreased to 4.4 V again, it is interesting to note that the discharge capacity increased from 54 (1st cycle) to ~80 mAh g<sup>-1</sup> (23rd cycle). It has been reported that the LMP particles experience significant volume changes during cycling attributed to the Jahn–Teller distortion and/or spin-state transition of  $\text{Mn}^{3+}$  [23]. Considering the substantial lattice distortions, it is plausible that the LMP-Pol-C (SP) particles may be exposed to more electrolyte as a result of surface cracking after significant lithium extraction from the lattice by increasing the cut-off voltage up to 4.8 V. This will allow previously inactive LMP in the core of a particle to become usable (activated) and become involved in electrochemical reactions. The nature of the mechanism for this increasing capacity will be addressed in a future study. After the 28th cycle, the applied current densities were increased from 8.55 to 34.2 mA g<sup>-1</sup>. As a result, discharge capacities decreased from ~80 to ~70 mAh g<sup>-1</sup> using a 4.4 V cut-off; and from ~110 to ~95 mAh g<sup>-1</sup> using a 4.8 V cut-off.

#### 4. Conclusions

The LMP-Pol showed flower-like morphology, with assemblies of platelets grown exposing the *bc*-plane as evidenced by TEM analysis. Regarding the  $\text{Li}^+$  diffusion pathway along the *b*-axis direction, a reduction of the  $\text{Li}^+$  diffusion length by decreasing average particle size is critical to the battery performances. The LMP-Pol needs to be further optimized by conductive carbon in intimately mixed composites to overcome the intrinsic insulating

properties of LMP. For example, the smallest particle size and the best specific capacity performance were achieved with polyol-produced LMP in combination with super-P carbon black (LMP-Pol-C (SP)) in comparison to the LMP/C composite (LMP-SSR-C) prepared by SSR method. AC-impedance measurements for the LMP-Pol-C (SP) cathode showed evidence of an increase in impedance after 50% delithiation, indicative of a difficult charging process. Because of this, the specific discharge capacity was strongly influenced by the upper cut-off voltage used during cycling; from ~50 mAh g<sup>-1</sup> at 4.4 V to ~120 mAh g<sup>-1</sup> at 4.8 V.

Through this study a better understanding of the LMP system was attained, in particular the additional challenges presented by the presence of the  $\text{Mn}^{3+}$  cation and the impact of Jahn–Teller distortions on electrochemical performance. It is apparent from this study that there are several issues that must be addressed for LMP to be considered as a feasible candidate for the positive electrode material for automotive applications such as slow charge rates and difficulty in obtaining homogeneous LMP-C nano-sized composite.

#### Acknowledgements

The authors would like to thank Bob R. Powell of the Chemical & Materials Systems Laboratory and Mark F. Mathias of the Electrochemical Energy Research Laboratory for many helpful discussions. The authors would also like to thank Curtis Wong and Michael P. Balogh of the Chemical & Materials Systems Laboratory for taking the SEM and TEM images, respectively. The research at Oak Ridge National Laboratory's Spallation Neutron Source was sponsored by the Scientific User Facilities Division, Office of Basic Energy Sciences, U.S. Department of Energy.

#### References

- [1] L.-X. Yuan, Z.-H. Wang, W.-X. Zhang, X.-L. Hu, J.T. Chen, Y.-H. Huang, J.B. Goodenough, Energy Environ. Sci. 4 (2011) 269–284.
- [2] R. Amin, P. Balaya, J. Maier, Electrochim. Solid State Lett. 10 (2007) A13–A16.
- [3] S.K. Martha, B. Markovsky, J. Grinblat, Y. Gofer, O. Haik, E. Zinigrad, D. Aurbach, T. Drezen, D. Wang, G. Deghenghi, I. Exnar, J. Electrochim. Soc. 156 (2009) A541–A552.
- [4] D. Morgan, A. Van der Ven, G. Ceder, Electrochim. Solid State Lett. 7 (2004) A30–A32.
- [5] N. Ravet, M. Gauthier, K. Zaghib, J.B. Goodenough, A. Mauger, F. Gendron, C.M. Julien, Chem. Mater. 19 (2007) 2595–2602.
- [6] T. Drezen, N.-H. Kwon, P. Bowen, I. Teerlinck, M. Isono, I. Exnar, J. Power Sources 174 (2007) 949–953.
- [7] C. Feldmann, Adv. Func. Mater. 13 (2003) 101–107.
- [8] A.V. Murugan, T. Muraligand, A. Manthiram, J. Electrochim. Soc. 156 (2009) A79–A83.
- [9] Y. Mizuno, M. Kotobuki, H. Munkakta, K. Kanamura, J. Ceram. Soc. Jpn. 117 (2009) 1225–1228.
- [10] T. Muraligand, A. Manthiram, J. Phys. Chem. C 114 (2010) 15530–15540.
- [11] J. Wang, X. Sun, Energy Environ. Sci. 5 (2012) 5163–5185.
- [12] A.C. Larson, R.B. von Dreele, General Structure Analysis System (GSAS) (2000). Los Alamos National Laboratory Report LAUR. p. 86748.
- [13] B.H. Toby, J. Appl. Crystallogr. 34 (2001) 210–213.
- [14] J. Stadelmann, JEMS. Retrieved from: <http://cimewww.epfl.ch/people/stadelmann/jemswebsite/jems.html>.
- [15] P.W. Stephens, J. Appl. Cryst. 32 (1999) 281–289.
- [16] J. Chen, S. Wang, M.S. Whittingham, J. Power Sources 174 (2007) 442–448.
- [17] K.-F. Hsu, S.-K. Hu, C.-H. Chen, M.-Y. Cheng, S.-Y. Tsay, T.-C. Chou, H.-S. Sheu, J.-F. Lee, B.-J. Hwang, J. Power Sources 192 (2009) 660–667.
- [18] D. Choi, D. Wang, I.-T. Bae, J. Xiao, Z. Nie, W. Wang, V.V. Viswanathan, Y.J. Lee, J.-G. Zhang, G.L. Graff, Z. Yang, J. Liu, Nano Lett. 10 (2010) 2799–2805.
- [19] J.-M. Tarascon, M. Morcrette, J. Saint, L. Aymard, R. Janot, C. R. Chim. 8 (2005) 17–26.
- [20] Timcal (2005) Retrieved Feb. 12, 2012, from: <http://www.timcal.com/scopi/group/timcal/timcal.nsf/pagesref/SCMM-7EVDTT?OpenDocument&lang=en>.
- [21] J.K. Hong, J.H. Lee, S.M. Oh, J. Polym. Soc. 111 (2002) 90–96.
- [22] A. Kay, U.S. Patent No. US2011/0012067 A1 (2011).
- [23] M. Kopeć, A. Yamada, G. Kobayashi, S. Nishimura, R. Kanno, A. Mauger, F. Gendron, C.M. Julien, J. Power Sources 189 (2009) 1154–1163.
- [24] Z. Bakenov, I. Taniguchi, J. Power Sources 195 (2010) 7445–7451.